

Multispectral transmission through phoxonic crystal slot-waveguide at midwave infrared frequencies

Anurag Sharma^{a,b}, Jyoti Kedia,^{a,*} and Neena Gupta^a

^aPunjab Engineering College (Deemed to be University), Chandigarh, Punjab, India

^bOptical Allied and Engineering Pvt. Ltd., Bangalore, Karnataka, India

Abstract. We design a multispectral transmission waveguide based on phoxonic crystals at midwave infrared (MWIR) frequencies. The phoxonic crystal slot-waveguide architecture is realized using a germanium (Ge)-slot waveguide, surrounded by a supercell array of oxide holes in silicon-germanium (SiGe) membrane tailored photonic and phononic crystal bandgap. The plane wave simulations for both photonic and phononic crystal unit cells were performed to confirm the geometry of the phoxonic supercell. The bandgap analysis shows the capability of the proposed architecture to confine photons of the terahertz frequency range within the slot waveguide by isolating them from the phonons of gigahertz frequency range. The phononic and photonic bandgaps were simultaneously engineered by varying the periodic variation of the density function and dielectric permittivity, respectively. The computational approach shows the suppression in photon-phonon scattering as validated by a uniform transmission of ~99.8% over a broad range of 3 to 5 μm wavelengths. The designed phoxonic crystal waveguide can be fabricated with planar processing technology and used in many applications where multispectral control of mid-IR signals is required. © 2023 Society of Photo-Optical Instrumentation Engineers (SPIE) [DOI: [10.1117/1.OE.62.4.047101](https://doi.org/10.1117/1.OE.62.4.047101)]

Keywords: phoxonic nanostructures; waveguides; cavity; optomechanics; midwave infrared; sensing.

Paper 20221178G received Oct. 10, 2022; accepted for publication Feb. 27, 2023; published online Apr. 5, 2023.

1 Introduction

Over the recent decade, multispectral waveguides have attracted significant interest because of their promising applications in quality monitoring,¹ remote sensing,² solar concentrator,^{3,4} multispectral imaging,^{5,6} and those requiring full on-chip integration, such as solid-state LIDAR and near-AR/VR displays.⁷⁻⁹ While most of the existing works related to multispectral transmissions are limited to the conventional telecommunication frequency spectrum, very few have demonstrated such broadband performance over midwave infrared (MWIR) frequencies while compromising with low optical transmission levels due to the associated nonlinear photon-phonon scattering losses.¹⁰⁻¹⁵ Further, recent reports have shown methodologies to dynamically control the simultaneously engineered transmitting frequency range. Such dynamic control is because of the manipulation of nonlinear photon and phonon dispersion characteristics as a function of periodically varying dielectric permittivity (photonic crystals) and the material's density (phononic crystals). The combined use of both photonic and phononic crystals leads to an emerging resonating waveguides based on phoxonic crystals (PxC), a subclass driven from cavity-optomechanics (C-OM).¹⁶⁻²²

Phoxonic crystal is a type of periodic nanostructure known to demonstrate unique properties based on the way they interact with both electromagnetic and elastic waves. These are known to exhibit simultaneous photonic and phononic band gaps for the propagation of electromagnetic and elastic waves in both linear as well as nonlinear mediums. The development of such periodic nanostructures has led to the realization of many micron and nanoscale devices so as to serve the low-energy applications. PxCs are recently known to form the basis for realizing various modern

*Address all correspondence to Jyoti Kedia, jyotikedia@pec.edu.in

optical phenomena like slow and fast light,²³ zero refractive index,¹⁶ chirality,²⁴ etc., and has proved to be a potential candidate in building nanoscale devices for measurements as precise as that of a small amount of mass or charge or even the ultra-short distance.^{25–27} While inserting defects into PxC arrays to form a cavity or a waveguide,²⁸ their ability to manipulate localized modes for both photons and phonons outshines. Such a possibility of high mode confinement within small volumes anticipates an ultra-strong nonlinear interaction for the purpose of the novel cavity-optomechanical (C-OM) devices and applications. Recently, technology platforms like silicon on insulator (SOI),²⁹ germanium on insulator (GOI),¹⁴ indium phosphide (InP),³⁰ and Ge-rich SiGe^{10,11,15,31} (silicon–germanium) with waveguide topologies like rib/ridge,³² suspended,^{33,34} and self-collimated virtual PxC have theoretically as well as experimentally, shown considerable improvement in the direction of achieving low-loss, multispectral on-chip MWIR transmission. Despite the flexibility that these waveguide platforms offer, the mandatory condition to have high refractive index contrast between core and cladding limits them to have minimum propagation losses at one or two wavelength peaks. It was discussed in previous review work³⁵ that the low-intensity MWIR light is highly scattered in nature. Due to this, it propagates non-uniformly through the small on-chip waveguides, which makes it very challenging to achieve multispectral transmission. Here, the nonuniform propagation actually implies to randomly vibrating mechanical (or phononic) frequency modes due to the compromise between high-refractive index contrast and mechanical strength between core and cladding.³⁵ Further, the MWIR wavelengths are propagated as thermally-incoherent radiations³⁶ and the randomly vibrating phonons results in moving-boundaries of a waveguide.³⁷ Such incoherence makes it difficult to propagate photons of a multiple wavelengths with similar transmission levels as they are more likely to get scattered by phonons. Such a nonuniform photon-phonon scattering leads to uncontrolled propagation of light. To have a multispectral on-chip propagation of photons with uniform transmission levels first, the source field must uniformly confine within the boundaries to provide unperturbed refractive index needed for low-loss waveguiding. Therefore, the source was analytically modeled as a function of material density function to have a uniform distribution of a complex MWIR source from 3 to 5 μm . In addition, choice of material is also very critical when changing the operating wavelength. So, the care was also taken to choose a supporting (or cladding) material with potential to compensate for both low-scattering losses as well as having the uniform optical transmission over a broad range of frequencies. Basically, the need was to have a cladding material that could provide sufficient mechanical strength to suppress the random phonons while have the uniform transparency for MWIR photons. The germanium (Ge) is well known for its better MWIR transparency¹⁴ while Ge-rich silicon–germanium (SiGe) is also known to have very strong thermal and mechanical stability along with broad optical transmission up to 11 μm .¹⁵ Thus, having the superior optomechanical strength due to high material density, better lattice match, and low-refractive index contrast with germanium, the experimentally¹⁵ grown $\text{Si}_{0.7}\text{Ge}_{0.3}$ film with 30% germanium concentration is one of the best choices. The refractive index data for experimentally grown, strain-induced SiGe (graded with 30% Ge) thin-film was provided by Montesinos-Ballester et al.¹⁵

Finally, a phoxonic crystal slot-waveguide architecture is proposed in this work, in which a 1×1.4 (μm) germanium core is sandwiched between a mirrored phoxonic crystal pair of oxide holes in SiGe membrane. From the macroscopic view, the incident (or pump) photons are impeding on to the waveguiding medium in a continuum. However, the microscopic view makes it necessary to understand the quantum mechanics involved in whole process. Here, each pump photon can be seen as interacting with the medium and resulting in the formation of a resultant (or stokes) photon along with the randomly vibrating phonons. Knowing that the magnitude of a phonon field represents any change in the shape and phase represents a change in the direction of momentum transfer of the phonon.³⁸ By suitable means to control the magnitude and phase of random phonons, it is thus possible to suppress the photon-phonon scattering effect and hence enhance the photon transmission levels. The QuTiP³⁹ (an open-source python package) was first used to verify the quantum dynamics for proposed COM-system interacting with thermal density perturbations modeled as a coherent source to excite the resonating membrane. After validating the source model and given the phonon to photon velocity contrast in SiGe membrane of the order of $\sim 10^5$ m/s, the plane-wave expansion module available with commercial design tools, viz., Lumerical and COMSOL, respectively, were then used to perform the simultaneous two-

dimensional (2D) photonic and phononic bandgap simulations.⁴⁰ The bandgap analysis is performed to optimize the hole-radius, which could help sustain the terahertz photons within the slot region while preventing the gigahertz phonons to laterally interact with those photons, which may cause them to scatter. With focus on lateral phonon momentum and given the limited computational resources, the independent 2D bandgap simulations were used initially to approximate the geometry parameters of both oxide holes. The resultant Eigen-mode frequencies of concern were then used to compute the Eigenmode solution for the complete supercell and hence observe the nature of mode shapes at those frequencies. Knowing that the final geometry is expected to cancel all other (flexural or toroidal) phonon modes except the longitudinal ones for the waveguiding application.^{41–44} The use of 2D bandgap analysis to select the final 3D structure is recommended here as a fast approximation method given the limited computational resources. The 2D-simulations resulted in extracting the feasible geometric parameters for the Holes-in-SiGe membrane to forbid the propagation of gigahertz (10^9) phonons and terahertz (10^{14}) photons. Finally, the three-dimensional (3D) finite-difference time-domain (FDTD) simulations of complete PxC-slot waveguide, excited by the thermally-coherent MWIR (3 to 5 μm) source show the uniform transmission characteristics over the entire wavelength range with ultra-low transmission loss up to 0.1 to 0.25 dB/cm. We have discussed in detail the influence of the geometric parameters of the PxC unit cells, which can be easily fabricated even with planar processing technology.

2 Materials and Methods

The schematic view of our multispectral PxC waveguide is illustrated in Fig. 1, which is based on a slot waveguiding architecture. The waveguide structure is built on top of conventional SOI substrate described computationally by defining perfectly matched layer (PML) boundary conditions. We optimize the performance of the 1 μm wide, germanium (Ge)-slot waveguide by surrounding it with a phoxonic crystal array constituting a combination of oxide holes (radius $[R, r]$; $R = 2r$; $R = 0.26 \pm 0.025 \mu\text{m}$; refer Fig. 1(a)] inscribed in $\text{Si}_{0.7}\text{Ge}_{0.3}$ slab with a 1.4 μm thickness $[t]$, refer Fig. 2(c)]. The experimental data for the $\text{Si}_{0.7}\text{Ge}_{0.3}$ layer was taken from M. Ballester's research group in ETH Zurich.¹⁵ The hole radius was optimized using particle swarm algorithm to compute the reflection spectra under the normal incidence of transverse electrically

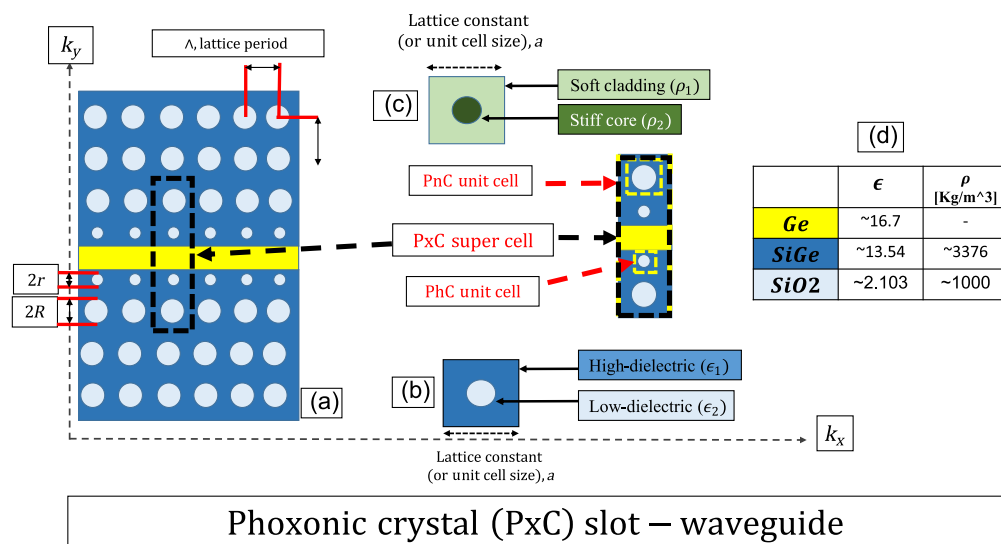


Fig. 1 The schematic of the proposed (phoxonic crystal) PxC waveguide device. (a) Top-view of the full architecture composed of germanium slot replacing the line defect in a (b) PhC unit cell and surrounded by (c) SiGe- PnC unit cell with oxide inclusions (or holes) of radius r and $R = 2r$, respectively, on both sides with a rectangular-lattice arrangement; (d) material description with optomechanical properties.

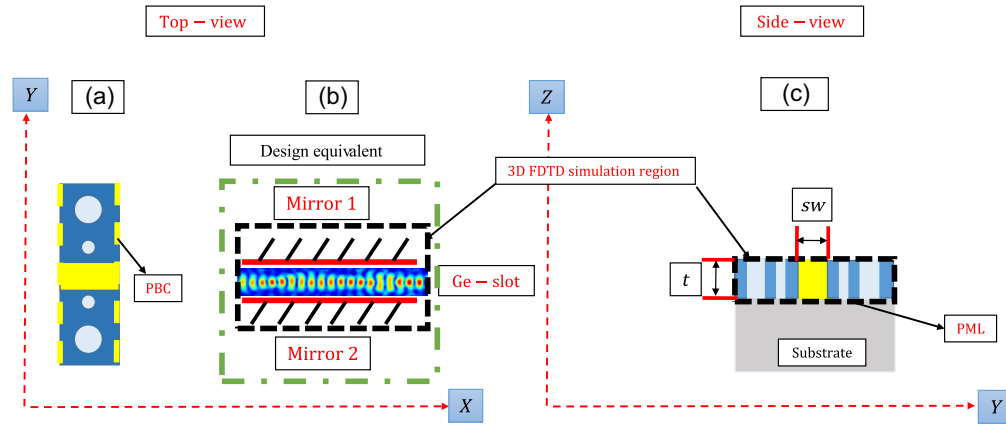


Fig. 2 The schematic of the proposed PxC. (a) Top-view of unit-cell (periodic in x-axis) with periodic boundary condition (PBC) in the direction of propagation; (b) Design equivalent schematic and (c) 2D side-view cross-section: with thickness, $t = 1.4 \mu\text{m}$ and slot-width, $sw = 1 \mu\text{m}$; with PML boundary-condition at upper and lower z-boundaries as well as left and right y-boundaries; The 3D FDTD waveguide simulation region is marked with dotted black lines in both (b) and (c).

(TE) polarized plane wave, available in both ANSYS and COMSOL FDTD modules to generate desired photonic and phononic bandgap frequencies. The computed bandgap frequency (f) is generally normalized with respect to the lattice constant, a . The lattice constant [Figs. 1(b) and 1(c)] refers to the smallest physical dimension of the unit cell in a crystal lattice while the lattice periodicity [Fig. 1(a)] is the minimum distance at which the lattice repeats itself. The lattice periodicity may be equal to or greater than the lattice constant for a uniformly spaced periodic structure. The silicon–germanium was chosen because of its large stiffness because of high mass density ($\sim 3376.75 \text{ kg/m}^3$) as well as dielectric permittivity of ~ 13.5 [see Fig. 1(d)], sufficient to provide the low-refractive index contrast to germanium slot for suppressing the photon–phonon (Brillouin⁴⁵) scattering loss. Out of the two main factors that we considered for the simultaneous tailoring of phoxonic crystal bandgap, one of them is the interdependence of the photon (Ph) and phonon (Pn) wavenumber (k) on their respective lattice periodicity Λ_{Ph} and Λ_{Pn} . The other is the change in dielectric permittivity (ϵ) as a function of material density (ρ) fluctuations due to thermally-varying mass density (ρ) over the desired range of MWIR spectrum.

Based on the optimizations, the lattice constant (a) is kept equal to lattice periodicity (Λ); marked as

$$\left[\frac{k_{\text{Pn}}}{k_{\text{Ph}}} = \frac{2\pi/\Lambda_{\text{Pn}}}{2\pi/\Lambda_{\text{Ph}}} = \frac{\Lambda_{\text{Ph}}}{\Lambda_{\text{Pn}}} \right]. \quad (1)$$

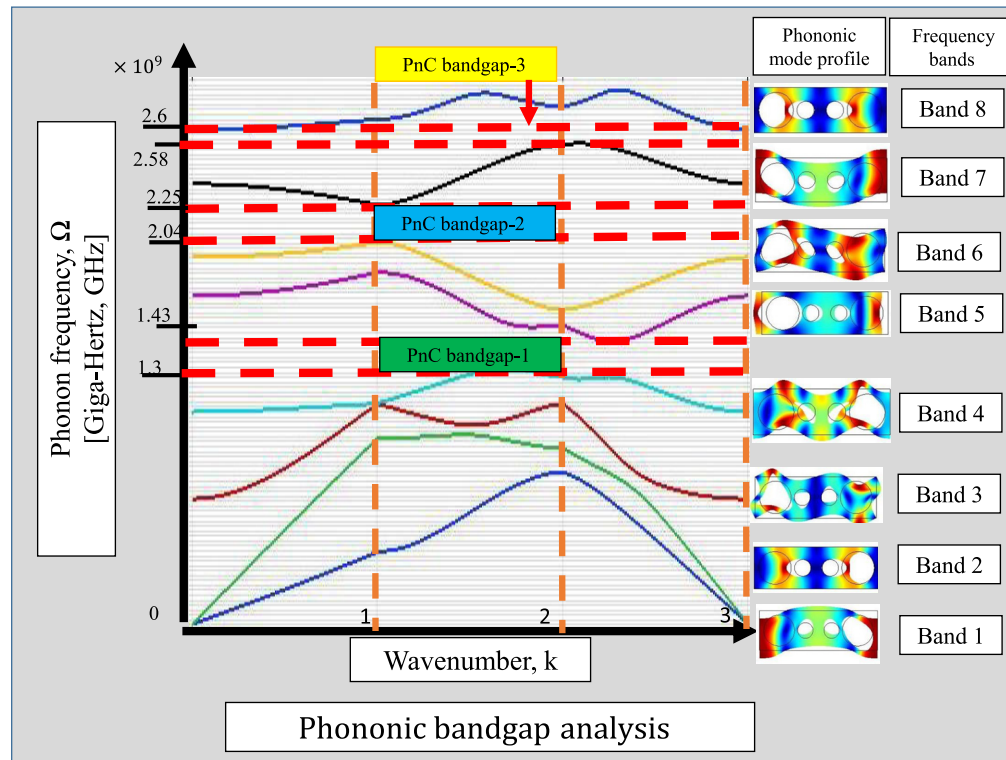
The following relation thus describes such an interdependence among the dielectric permittivity and material density can be defined as the electro-restrictive³⁷ coefficient (γ) of the phoxonic structure. This relation governs the functionality of refractive index variation and the stiffness contrast between core and cladding material

$$\gamma = \epsilon = \rho \frac{\partial \epsilon}{\partial \rho}. \quad (2)$$

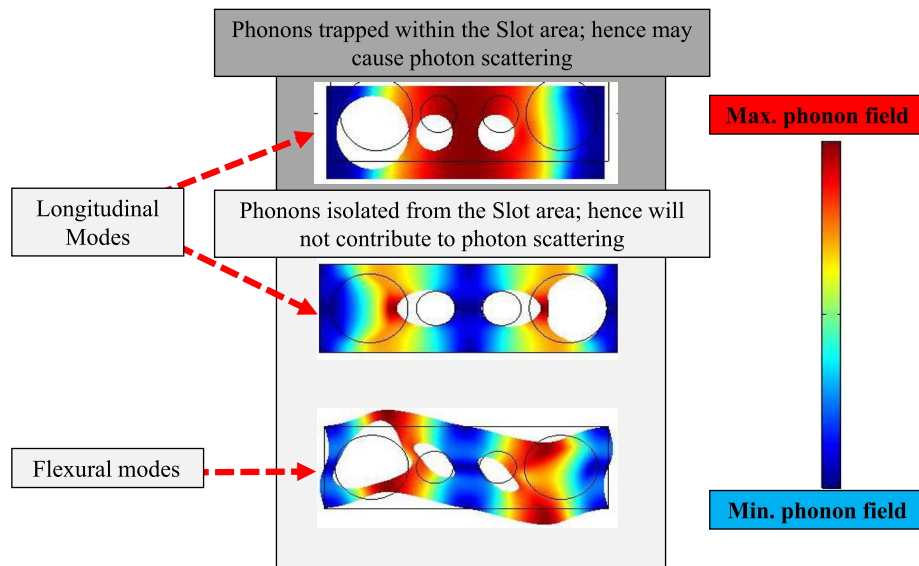
By examining the structural mode profiles of the PxC supercell [see equivalent schematic in Fig. 2(b)], the structure is made mirror symmetric across the slot waveguide to satisfy phase-matching condition⁴⁶ across the core boundaries.

3 Results and Discussions

On the basis of 2D FDTD numerical computations, we separately performed bandgap analysis of the photonic crystal followed by a phononic crystal unit-cell to optimize the geometry of an



(a)



(b)

Fig. 3 (a) The phononic frequency bandgap diagram for the proposed SiGe-PnC unit-cell with oxide holes showing three complete PnC bandgaps (1, 2, 3) with GHz-phonons forbidden in the slot region. (b) The eigenfrequency mode profile signifies the nature of the vibrations of a phononic waveguide either as flexural or longitudinal; the modes with the red portion in the slot region were observed at frequencies lying between PnC bandgaps (1, 2, 3), whereas the flexural or the weak longitudinal mode with blue color at the slot region are the mode shapes observed outside the PnC bandgap regions.

oxide hole through a $\text{Si}_{0.7}\text{Ge}_{0.3}$ membrane so as to be able to attain the desired THz and GHz forbidden frequency ranges. We considered the broadband MWIR source as thermally-radiating heat-flux (Ξ) modeled as $\Xi^2 = (\rho C_p T)^2 \tilde{u}_k^2$ in terms of the mass density (ρ), ambient temperature (T), specific-heat coefficient (C_p), and the boundary displacements (\tilde{u}) of the periodic boundaries represented as

$$\tilde{u}_{\text{final}} = \exp^{i k(r_{\text{final}} - r_{\text{initial}})} \tilde{u}_{\text{initial}}. \quad (3)$$

The initial and final subscripts represent the periodic boundary condition (PBC) applied at the opposite edges, see Fig. 1 with yellow dotted lines for PhC and PnC unit-cell and black for final PnC supercell [also shown in Fig. 2(a)] repeating in the direction of propagation. Such Floquet (or periodic) boundary conditions are used to save the simulation time and computational resources required for simulating an entire array. For the PnC super-cell structure shown in Fig. 2(a), we performed the two-dimensional (2D) phononic bandgap simulations to solve the boundary value problem using the Plane-wave expansion method⁴⁷ that results in two complete PnC bandgaps (1 and 2) as shown in Fig. 3. To achieve these, the matrix material features with an elasticity modulus of 2 GPa and a mass density (ρ_1): 1000 kg/m³ and SiGe as the core material with an elasticity modulus of 748 GPa and mass density (ρ_2) of 3376.75 kg/m³. Figure 3(b) shows the nature of eigen frequency modes of a phononic waveguide. The vibrational modes are mainly classified as longitudinal and flexural. Knowing the longitudinal modes as the simple standing wave modes, the flexural modes can be understood as a spatially modulated mode like rotation of the cross-sectional planes about the median longitudinal axis depicted in Fig. 3(b). The longitudinal modes with no vibrational energy loss are expected and observed over entire bandgap frequency range such that the germanium core can be placed in the slot region. The frequency bands marked in Fig. 3(a); see dotted lines with color green, blue, and yellow for complete PnC Bandgap-1 (1.3 to 1.43 GHz), Bandgap-2 (2.04 to 2.25 GHz), and Bandgap-3, respectively, corresponds to those desired mode profiles. Note that each band represents a particular eigen-frequency mode of the phonon field with maximum and minimum intensity shown by red and blue color, respectively. Similarly, the 2D-PhC unit-cell [mentioned in Fig. 1(d)] was independently optimized using RCWA (rigorous coupled wave analysis) and Plane-wave expansion (PWE) methods to verify the complete PhC bandgap ($f \times a/c$) (see Fig. 4) from 0.15 to 0.22 covering the desired THz frequency ranges. Following the above

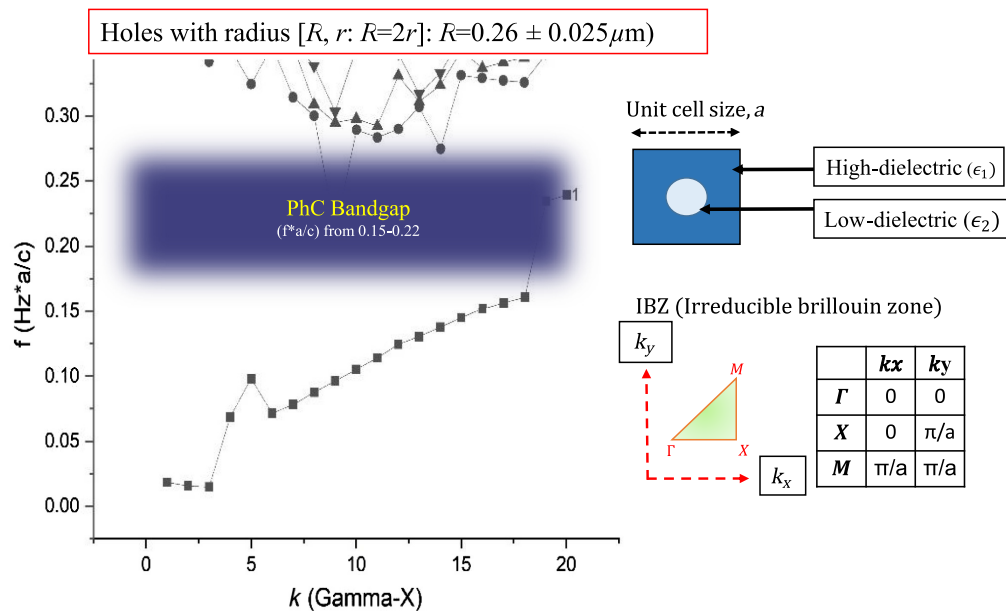


Fig. 4 The photonic frequency bandgap diagram for the SiGe-PhC unit cell: optimized for oxide holes of radius “ R ” and “ r ,” respectively, showing complete PhC bandgaps for wide range of THz-frequencies.

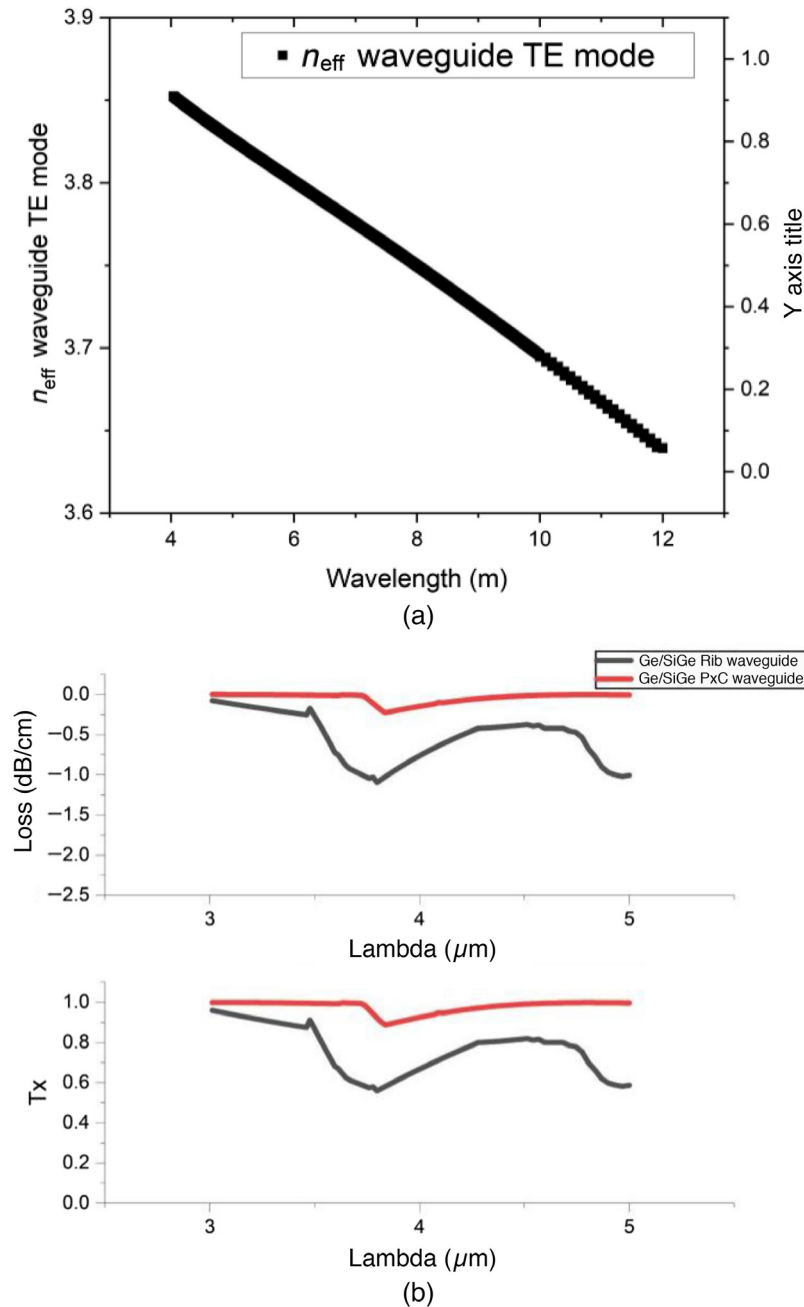


Fig. 5 (a) The effective refractive index of the proposed waveguide and (b) transmission characteristics of proposed waveguide architecture (red) compared with simple Rib waveguide architecture (black) show considerable reduction of loss.

bandgap analysis, the germanium core layer is then assigned to the slot region. Thereafter, we perform the waveguide simulations using Lumerical-FDTD algorithm for PxC super-cell [see Fig. 2(a)] repeating in the direction of wave propagation. The Ge-slot region is excited by the TE-polarized MWIR broadband source (3 to 5 μm or 60 to 100 THz) modeled as discussed above. As expected, the better confinement of the desired photons within the germanium slot was observed as confirmed by uniform transmission in Fig. 5 and waveguide mode profiles in Fig. 6. Figure 5(a) is the simulated effective refractive index of the proposed waveguide implicating the nature of fundamental TE mode of propagation. The FDTD waveguide simulations for PxC super-cell in comparison to the waveguide transmission performance with simple Rib type waveguide architecture are shown in Fig. 5(b). Thus, confirming better confinement of the

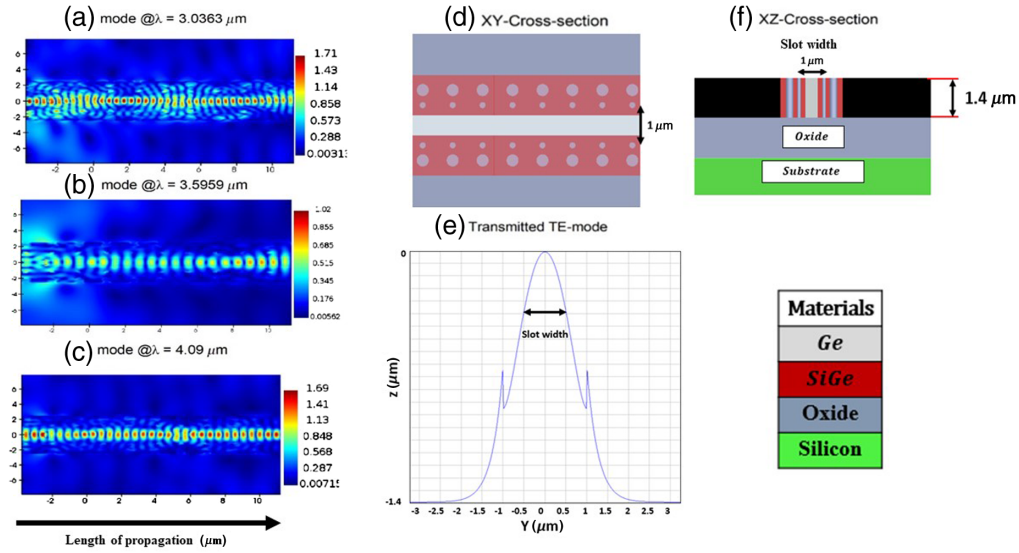


Fig. 6 The transmission profiles obtained by Ansys Lumerical FDTD-simulations of SiGe-phoxonic crystal Ge-Slot waveguide measured at peak wavelengths of (a) $3.0363 \mu\text{m}$, (b) $3.5959 \mu\text{m}$, and (c) $4.09 \mu\text{m}$ when excited by (e) the TE-polarized input multispectral source; finally, (d) the XY and (f) XZ-cross-section view of the proposed waveguide topology.

desired photons within the germanium slot, which is attributed to isolated phonon frequencies within PnC bandgap 1 and 2. It can be observed that the proposed structure shows uniform transmission compared to conventional Rib waveguide architectures as shown in Table 1. Such performance confirms the potential of phoxonic structures to realize an ultra-low loss, multispectral waveguiding solution if tailored with rigorous computations. The resultant electric field mode profiles as shown in Figs. 6(a)–6(c) further validates such a strong confinement for desired wavelength peaks when simulated by a broadband MWIR slab mode as shown in Fig. 6(e) being allowed to propagate through the slot-region. Note that we did get similar confinement for other wavelength peaks in the entire wavelength range from 3 to $5 \mu\text{m}$. Table 1 compiles the comparison of proposed waveguide with some of the recent works in terms of total transmission loss in dB/cm given by the following relation.

$$\text{Loss [dB/cm]} = 10 \times \log e \frac{\alpha}{L} = 4.34 \times \frac{\alpha}{L}. \quad (4)$$

However, the attenuation coefficient ($\alpha = -\log_{10} \frac{P}{P_0}$) being in dB/ μm , as it is numerically calculated for the given bandwidth as a function of the ratio of total transmitted power P_0 through the proposed waveguide and the received power P . The ratio is then normalized for 1 cm of waveguide length (L). The normalized attenuation coefficient to calculate the Loss [dB/cm] is rewritten as $\alpha = -\frac{1}{L} \log_{10} \frac{P}{P_0}$. For comparison, the most relevant and recent works related to the conventional waveguide architectures belonging to different technology platforms were chosen. It can be observed that one of the popular approaches i.e., suspending³³ the core from the bulk results in considerable reduction of the bulk scattering losses. However, such a reduction has only been observed either at single or dual wavelength peaks (6.4 or $8.5 \mu\text{m}$) with approximate bandwidth up to $3 \mu\text{m}$, using conventional waveguide architectures viz., Rib⁴⁸ and Ridge³¹ type. Despite being multispectral with large bandwidth, these devices however could provide transmission levels above 50% only for selective wavelength peaks. Thus, limiting the device performance for a particular type of application. So, the main aim of this study was to lead a way toward developing a waveguide architecture that could be used to provide sufficient transmission levels for an entire bandwidth. As per expectations, the proposed slot-waveguide architecture confirms high optical transmission levels ($>90\%$) for multiple wavelength peaks over an entire bandwidth of 3 to $5 \mu\text{m}$ as shown in Fig. 5(b). In particular, $\sim 99.8\%$ transmission level was observed at wavelength peaks of 3.0363 and $4.09 \mu\text{m}$. Such a device is expected to favor the

Table 1 The comparison table shows the comparison of proposed phoxonic crystal slot-waveguide with recent literature.

Reference	Technology	Waveguide architecture	Core (width × height) (μm)	Cladding support	Peak Wavelength (μm)	Bandwidth	Transmission Loss (dB/cm)
2018 ¹⁰	Graded SiGe on SOI	Rib	3.5 × 4	—	~6.4	5.4–8.4 (μm)	2–3
2020 ⁴⁸	Graded SiGe on SOI	Rib	6.2 × 6.1	—	~8.5	7.5–9.4 (μm)	2–20
2021 ³³	Si on SOI	Suspended Rib	1.4 × 0.5	SWGs (with 4 μm width with 0.4 μm thick air Holes varying periodically in direction of propagation with 0.6 μm period)	~4	3.7–4.1 (μm)	2.9
2022 ³⁰	InGaAs/InP	Ridge	3.5 × 7.5	—	~5.35	5–11 (μm)	0.5–4.5
Proposed work	Phoxonic crystal-based germanium on insulator	Slot	1 × 1.4	SiGe membrane with pair of oxide holes having radius $[R, r]$; and lattice constant, a $[0.4R, 0.288r]$	Multiple peaks	3–5 (μm)	0.1–0.25

on-chip waveguiding of low-intensity infrared light within small volumes. Therefore, the proposed computational model shows better performance by claiming uniform transmission levels over multiple wavelength peaks instead of having a superior performance only at single or dual peaks. The device can further be fabricated by either of the state-of-the-art facilities like nano-imprint or holography-based lithography.^{49,50} The work holds a huge scope in the development of economical low-loss, multispectral on-chip waveguides for taking a leap toward all-optical regime.

4 Conclusion

We have investigated the transmission and bandwidth performance of a slot-waveguide architecture at midinfrared frequencies based on phoxonic crystal nanostructures. We exploited the optical and mechanical properties of experimentally grown Ge (30%)-rich SiGe material to confine the optical radiations within the core. The proposed architecture is built with a germanium (Ge)-slot waveguide, surrounded by a supercell array of oxide holes in silicon-germanium (SiGe) membrane demonstrated the potential for multispectral photonic resonance modes, which is attributed to the suppression of the dominating photon-phonon scattering loss for the case of longer wavelengths. The waveguide was excited by a broadband MWIR source, modeled as the thermal density perturbations to periodic boundaries of core. The final FDTD calculations confirmed a better optical transmission with uniform of $\sim 99.8\%$ over entire 3 to 5 μm range unlike just the single or dual peak performance for conventional architectures. The designed PxC slot waveguide can be used in many applications where lossless multispectral transmission of MWIR signals is required like the emerging AR/VR waveguiding, Lidar sensing, and other noncontact sensing-based imaging and nonimaging applications.

References

1. K. Bougot-Robin et al., "A multispectral resonant waveguide nanopatterned chip for robust oil quality monitoring," *Sens. Actuators B* **216**, 221–228 (2015).
2. S. Nag et al., "Multispectral snapshot imagers onboard small satellite formations for multi-angular remote sensing," *IEEE Sens. J.* **17**(16), 5252–5268 (2017).
3. V. Kataria and D. S. Mehta, "Multispectral harvesting rare-earth oxysulphide based highly efficient transparent luminescent solar concentrator," *J. Rare Earths* **40**(1), 41–48 (2022).
4. S.-M. Lee et al., "Synergistically enhanced performance of ultrathin nanostructured silicon solar cells embedded in plasmonically assisted, multispectral luminescent waveguides," *ACS Nano* **11**(4), 4077–4085 (2017).
5. F. Rousset et al., "Time-resolved multispectral imaging based on an adaptive single-pixel camera," *Opt. Express* **26**(8), 10550–10558 (2018).
6. B. Crozier et al., "Controlling the light absorption in a photodetector via nanowire waveguide resonances for multispectral and color imaging," *IEEE J. Sel. Top. Quantum Electron.* **24**(6), 1–12 (2018).
7. Y. Ding et al., "Metasurface-dressed two-dimensional on-chip waveguide for free-space light field manipulation," *ACS Photonics* **9**(2), 398–404 (2022).
8. B. C. Kress, "Digital optical elements and technologies (EDO19): applications to AR/VR/MR," *Proc. SPIE* **11062**, 1106222 (2019).
9. T. Nielsen, "Waveguide and sensing technologies for AR/VR/MR," *Proc. SPIE* **11932**, 119320F (2022).
10. J. M. R. Amirez et al., "Graded SiGe waveguides with broadband low-loss propagation in the mid infrared," *Opt. Express* **26**(2), 528–531 (2018).
11. A. Sharma, J. Kedia, and N. Gupta, "Design of a SiGe waveguide photodetector with PxC cavity for broadband MWIR sensing," in *Workshop Recent Adv. Photonics (WRAP)*, IEEE (2022).
12. L. Carletti et al., "Mid-infrared nonlinear optics in SiGe waveguides," in *IEEE Summer Top. Meeting Ser. (SUM)*, IEEE (2015).

13. P. T. Lin et al., “Label-free water sensors using hybrid polymer–dielectric mid-infrared optical waveguides,” *ACS Appl. Mater. Interfaces* **7**(21), 11189–11194 (2015).
14. M. Nedeljkovic et al., “Germanium-on-silicon waveguides operating at mid-infrared wavelengths up to 8.5 μm ,” *Opt. Express* **25**(22), 27431–27441 (2017).
15. M. Montesinos-Ballester et al., “Optical modulation in Ge-rich SiGe waveguides in the mid-infrared wavelength range up to 11 μm ,” *Commun. Mater.* **1**(1), 6 (2020).
16. L. Lei et al., “Dirac cones with zero refractive indices in phoxonic crystals,” *Opt. Express* **30**(1), 308–317 (2022).
17. P. Moradi and A. Bahrami, “Design of an optomechanical filter based on solid/solid phoxonic crystals,” *J. Appl. Phys.* **123**(11), 115113 (2018).
18. A. H. Aly, S. M. Shaban, and A. Mehaney, “High-performance phoxonic cavity designs for enhanced acousto-optical interaction,” *Appl. Opt.* **60**(11), 3224–3231 (2021).
19. K.-Y. Li et al., “A high-sensitivity liquid concentration-sensing structure based on a phoxonic crystal slot nanobeam,” *J. Appl. Phys.* **131**(2), 024501 (2022).
20. H. Li et al., “Simultaneous unidirectional reciprocal filters of electromagnetic and elastic waves based on the modal symmetry of phoxonic crystal waveguides and cavity,” *Phys. Lett. A* **384**(20), 126499 (2020).
21. M. Tian et al., “Acousto-optical coupling of the side surface acoustic and optical waves in a two-dimensional phoxonic crystal slab hetero-structure cavity,” *Opt. Commun.* **513**, 128095 (2022).
22. Y. Shu et al., “Design of phoxonic virtual waveguides for both electromagnetic and elastic waves based on the self-collimation effect: an application to enhance acousto-optic interaction,” *Opt. Express* **28**(17), 24813–24819 (2020).
23. R. Faggiani et al., “Design of periodic waveguide for enhancing the interaction of light and atoms in a vacuum,” *Proc. SPIE* **10119**, 101190R (2017).
24. D. D. Sedov, V. K. Kozin, and I. V. Iorsh, “Chiral waveguide optomechanics: first order quantum phase transitions with Z 3 symmetry breaking,” *Phys. Rev. Lett.* **125**(26), 263606 (2020).
25. A. Doliveira et al., “Determination of a statistical lack of volume matter by resonance principle: experiential approach and modeling,” *Proc. SPIE* **11775**, 1177513 (2021).
26. B.-H. Wu et al., “Quantum computing with multidimensional continuous-variable cluster states in a scalable photonic platform,” *Phys. Rev. Res.* **2**(2), 023138 (2020).
27. N. Turk et al., “Waveguide-based surface-enhanced Raman spectroscopy detection of protease activity using non-natural aromatic amino acids,” *Biomed. Opt. Express* **11**(8), 4800–4816 (2020).
28. H. Gao et al., “Theoretical studies of dual optical and acoustic unidirectional filtering based on two-dimensional phoxonic crystals with rectangle defects,” *Fiber Integr. Opt.* **39**(5–6), 253–263 (2020).
29. S. A. Miller et al., “Low-loss silicon platform for broadband mid-infrared photonics,” *Optica* **4**(7), 707–712 (2017).
30. K. Zhang, G. Böhm, and M. A. Belkin, “Mid-infrared microring resonators and optical waveguides on an InP platform,” *Appl. Phys. Lett.* **120**(6), 061106 (2022).
31. S. Hansen et al., “A SiGe-chip-based D-band FMCW-radar sensor with 53-GHz tuning range for high resolution measurements in industrial applications,” *IEEE Trans. Microwave Theory Tech.* **70**(1), 719–731 (2021).
32. W. Du et al., “Study of Si-based GeSn optically pumped lasers with micro-disk and ridge waveguide structures,” *Front. Phys.* **7**, 147 (2019).
33. Q. Qiao et al., “Suspended silicon waveguide with sub-wavelength grating cladding for optical mems in mid-infrared,” *Micromachines (Basel)* **12**(11), 1311 (2021).
34. W. Wang et al., “A theoretical study of tunable brillouin lasers based on a diamond suspended waveguide,” *Front. Phys.* **10**, 913774 (2022).
35. A. Sharma, J. Kedia, and N. Gupta, “Emerging nanostructured infrared absorbers enabling cost-effective image sensing: a review,” *Opt. Eng.* **60**(9), 090901 (2021).
36. A. Sharma, J. Kedia, and N. Gupta, “Nanostructured material engineering for ultra-low loss MWIR thermal sensors—a short review,” *Mater. Today: Proc.* **28**, 1709–1713 (2020).
37. T. A. Huffman et al., “Integrated resonators in an ultralow loss Si 3 N 4/SiO 2 platform for multifunction applications,” *IEEE J. Sel. Top. Quantum Electron.* **24**(4), 1–9 (2018).

38. V. Laude et al., "Simultaneous guidance of slow photons and slow acoustic phonons in silicon phoxonic crystal slabs," *Opt. Express* **19**(10), 9690–9698 (2011).
39. J. R. Johansson, P. D. Nation, and F. Nori, "QuTiP: an open-source Python framework for the dynamics of open quantum systems," *Comput. Phys. Commun.* **183**(8), 1760–1772 (2012).
40. X. Ma et al., "Geometric parameters optimization of a two-dimensional phoxonic crystal with dual forbidden band characteristics," *Mod. Phys. Lett. B* **36**(04), 2150561 (2022).
41. B. Chouvion et al., "Vibration modelling of complex waveguide structures," *Comput. Struct.* **89**(11–12), 1253–1263 (2011).
42. B. R. Mace, "Active control of flexural vibrations," *J. Sound Vib.* **114**(2), 253–270 (1987).
43. L. Friis and M. Ohlrich, "Coupled flexural-longitudinal wave motion in a finite periodic structure with asymmetrically arranged transverse beams," *J. Acoust. Soc. Am.* **118**(6), 3607–3618 (2005).
44. D. Hümmer et al., "Heating in nanophotonic traps for cold atoms," *Phys. Rev. X* **9**(4), 041034 (2019).
45. C. Wolff et al., "Brillouin scattering—theory and experiment: tutorial," *JOSA B* **38**(4), 1243–1269 (2021).
46. G. S. Wiederhecker, P. Dainese, and T. P. Mayer Alegre, "Brillouin optomechanics in nanophotonic structures," *APL Photonics* **4**(7), 071101 (2019).
47. C. J. S. Alves et al., "Solving boundary value problems on manifolds with a plane waves method," *Appl. Math. Lett.* **107**, 106426 (2020).
48. M. Montesinos-Ballester et al., "On-chip mid-infrared supercontinuum generation from 3 to 13 μm wavelength," *ACS Photonics* **7**(12), 3423–3429 (2020).
49. J. L. Zhang and T. F. Kuech, "Fabrication and properties of an asymmetric waveguide containing nanoparticles," *J. Electron. Mater.* **37**, 135–144 (2008).
50. S.-W. Ahn et al., "Fabrication of a 50 nm half-pitch wire grid polarizer using nanoimprint lithography," *Nanotechnology* **16**(9), 1874 (2005).

Anurag Sharma is an optics and photonics design scientific research engineer at Optics Allied and Engineering Private Ltd., Bangalore, India. He received his BE degree in ECE from Himachal Pradesh University, Shimla, India, in 2013, his master's degree from Chandigarh University, Punjab, India, in 2016, and is pursuing his PhD in ECE with majors in optics and nanophotonics at Punjab Engineering College (deemed to be University) Chandigarh, India, since 2018. He worked as assistant professor at Chandigarh University, Punjab, India, from 2016 to 2018. His areas of research include nanophotonic sensing, integrated photonics, macro-optics, AI-enabled computational device modeling, diffraction optics, meta-materials, and analog VLSI design. He is a student member of SPIE-CSIO Chapter, Optica Technical Group (OSA), and IEEE Photonics Consortium of India.

Jyoti Kedia received her master's degree from Thapar University and her PhD in optical communication from Punjab Engineering College (deemed to be University), India, 2004 and 2017, respectively. She is an assistant professor in the ECE Department, Punjab Engineering College (deemed to be University) Chandigarh, India. Her research interests include optical sensors, passive optical networks, integrated optics, photonics, optical sensors, and VLSI. She has published more than 40 research/technical papers in various international/national journals and conferences.

Neena Gupta received her BE degree in electronics and communication engineering (ECE), her ME degree in electronics, and her PhD in optical communication from Punjab University in 1988, 1992, and 2002, respectively. She is a professor at the ECE Department, Punjab Engineering College (deemed to be University) Chandigarh, India. She is a senior member of IEEE, having vast teaching and research experience. Her research interests focus on optical communication. She has contributed to various journals and conferences.